

# Ultra-Wideband Featuring Enhanced Delay and Sum Algorithm and Oriented for Detecting Early Stage Breast Cancer

Mohammed S. Hathal<sup>1, \*</sup>, Suhair S. Salih<sup>2</sup>, and Alaa H. Hasan<sup>2</sup>

**Abstract**—In this study, we present the experimental results of ultra-wideband (UWB) imaging oriented for detecting small malignant breast tumors at an early stage. The technique is based on radar sensing, whereby tissues are differentiated based on the dielectric contrast between the disease and its surrounding healthy tissues. The image reconstruction algorithm referred to herein as the enhanced version of delay and sum (EDAS) algorithm is used to identify the malignant tissue in a cluttered environment and noisy data. The methods and procedures are tested using MRI-derived breast phantoms, and the results are compared with images obtained from classical DAS variant. Incorporating a new filtering technique and multiplication procedure, the proposed algorithm is effective in reducing the clutter and producing better images. Overall, the methods and procedures registered a signal-to-clutter ratio (SCR) value of 1.54 dB when imaging the most challenging example involving the heterogeneously dense model in 8-antenna geometry. The SCR is slightly increased to 3.12 dB when the number of sensors is increased to 16.

## 1. INTRODUCTION

The past decade has seen the emergence of new but innovative imaging technique based on radar sensing applicable to medical application, particularly in breast cancer diagnosis [1], as well as to civil engineering structures [2, 3]. Consequently, several researches have focused on radar imaging because it allows image reconstruction to be executed in a single step rather than formerly solving the inverse problem. Resolving the inverse problems can be difficult particularly in cases of noisy or incomplete dataset. There are various reasons for the incomplete dataset. Prominent among them is the use of limited number of sensors due to space restriction of the area under investigation or the presence of obstacles on its surface. Moreover, the problem is often ill-posed, in which small errors in the data can lead to large errors in the solution. This is especially true with breast sensing because of the cluttering generated by the heterogeneity of the healthy tissue surrounding the cancerous cells, which causes multi-scattering effects. Therefore, the iterative nonlinear solvers often result in divergence of otherwise convergent algorithm [4]. In contrast, the convergence of the radar-based algorithm is always guaranteed, since the inversion is based on direct approach instead of matrix minimization. However, the image that it produces is qualitative instead of quantitative as in the iterative approach. This trade-off is acceptable in certain specialized applications like the breast mapping in which detection is sufficiently adequate for early diagnosis. The strategy of radar-based image reconstruction technique relies on dielectric contrast between malignant and normal tissues [5]. UWB radar based techniques aim to identify the presence and location of significant scattered energy arising from the dielectric variation. These techniques, do not solve the inverse problem, and therefore, are less demanding computationally. An example of radar-type approach is the delay and sum (DAS) algorithm, which was first proposed by Hagness in 1998 [1, 6].

---

*Received 28 January 2020, Accepted 7 November 2020, Scheduled 18 January 2021*

\* Corresponding author: Mohammed Sadoon Hathal (mshm73@gmail.com).

<sup>1</sup> Department of Computer Engineering, College of Engineering, University of Baghdad, Baghdad, Iraq. <sup>2</sup> Department of Medical Analysis, AL-Farabi University College, Baghdad, Iraq.

In literature, this technique is also referred to as confocal microwave imaging (CMI). Generally, CMI focuses only on significant scatterings instead of quantitatively calculating the dielectric properties of the entire breast. Solving this problem generally requires time alignment of the coherently mapped arrival pulses and filtering a strong artifact and noise to improve image qualities. Nevertheless, the original version of this algorithm offers limited capability in terms of clutter suppression and artifacts [7]. As stated by these authors, the CMI is very effective in filtering simple type of artifacts like reflections at skin-breast interface and antenna coupling. This is because this technique employs relatively simple filtering technique based on time shifting and signal addition. A more advanced approach is needed in order to deal with other types of artifacts especially the clutter generated by the complex in-homogeneity of breast tissues. Recent research on microwave image reconstruction for CMI method has evolved into two tracks: data-dependent [8] and data-independent methods [9]. Multi-static adaptive microwave imaging (MAMI) [10] is a data-dependent method that utilizes a robust Capon beamformer (RCB) [11] to correct errors in the steering vector resulting from dispersive propagation effects. Although the results are quite promising, the accuracy of this algorithm relies strongly on an accurate estimation of the steering vector, whose computational complexity increases as the heterogeneity of the media increases. Meanwhile, the data-independent reconstruction methods do not depend on steering vector information and are mainly based on the standard DAS beam-forming technique [1, 6]. The method uses simple time-shifting and adding (synthetic focusing) of backscattered energy to reconstruct the image. As a result, this method is less computationally intensive. Based on the assumption that breast tissue is principally homogeneous, researchers have incorporated numerous advances to DAS resulting in the development of several variants [12–17]. However, the original DAS including its variants has one principal drawback that it assumes that there is a significant contrast between cancerous and normal breast tissues. Theoretically, this assumption is valid for certain types of breast, namely the fatty breast in which the homogeneous tissue constitutes more than 80% of the breast composition [18]. For other types of breast, particularly the heterogeneous dense breast that is composed of scattered fibroglandular structure in addition to fatty tissue, this assumption does not hold since the dielectric contrast between healthy and cancerous cells can be as low as 1 : 1.7 [19]. Therefore, a direct application of these techniques would result in noisy reconstruction. Furthermore, the reduction of the permittivity contrast can lead to both glandular and cancerous tissues appearing as high pixel energy in the tomogram, hence, raising the possibility of a false-positive diagnosis [18]. This depicts a more complex imaging scenario and instigates the development of improved signal processing techniques for UWB sensing.

In an effort to further improve the capability and capacity of the DAS algorithm, especially for the accurate detection of early stage malignant tumor in human breast, an enhanced version of the delay and sum (EDAS) algorithm, featuring multi-static measurement geometry, has been developed and tested in our laboratory. The preliminary results obtained from simulations and laboratory experiments suggest that the proposed algorithm is effective in reducing the clutters and improving the image-to-signal ratio. In this paper, the performance and accuracy of this algorithm is further evaluated in the most challenging scenario using the densely heterogeneous breast models. The results are compared with conventional beam forming algorithm, from which the conclusions are derived.

## 2. IMAGE RECONSTRUCTION

The UWB radar imaging technique aims to reconstruct the presence and location of the scattered signature arising from the dielectric contrast between malignant and surrounded breast tissues. Therefore, the qualitative image is displayed as a variance of energy intensity. For a UWB radar, a transmitting antenna sends a very short-duration pulse of microwave energy, which penetrates into the region under test and becomes scattered by any target that exhibits variation contrast in dielectric properties. The receiving antennas record these scattered signals from which the target non-homogeneities are reconstructed.

### 2.1. The Delay and Sum (DAS)

The DAS monostatic approach was developed by Nilavalan et al., to multistatic measurements [12]. In this technique, the object is illuminated sequentially from a number of sensor locations. For each

transmitter, the signals arriving at other sensors are sequentially recorded. Thus, gathering more information from the imaging scene. The distance from each transmitting sensor position to point of interest  $r$  and back to the receiving sensor position is calculated. The calculation is based on the speed of propagation, and the results are converted into time delays. Then, the recorded signals are time shifted, summed to calculate the energy at each point of interest.

The energy value of the synthetic focal point  $r$  is obtained through the integration of contributions over a time window  $w$ :

$$En(r) = \int_0^w \left[ \sum_{m=1}^M \sum_{n=1}^N x_{m,n}(t - \tau_{m,n}(r)) \right]^2 dt \quad (1)$$

where  $x_{m,n}$  is the back scattered signal recorded from the  $n$ th receiver when the  $m$ th antenna is transmitting,  $\tau_{m,n}$  the time delay, and  $t$  the time. The propagation delay time is defined as:

$$\tau_{m,n}(r) = \frac{\|r - r_m\| + \|r - r_n\|}{v\Delta t} \quad (2)$$

where  $\|r - r_m\|$  and  $\|r - r_n\|$  are the distances between the focal point  $r$  and antennas, and  $v$  is the velocity of propagation.

## 2.2. The Enhanced Delay and Sum (EDAS)

The proposed EDAS algorithm is similar to DAS algorithm but incorporates a hybrid processing technique combining (i) the weighted coherence factor ( $CF$ ) and (ii) the multiplication procedure. In doing so, the round-trip traveling time from each antenna to the focal point is first calculated, generating the backscattered signals with an appropriate time delay. This process is repeated until all focal points have been scanned, and the time delay corresponding to each focal point and for a given transmitter-receiver position has been calculated. Second, the backscattered signals from the tumour are combined and added coherently to produce maximum energy at a given focal point. In the absence of a tumour, backscattering from breast tissue would add up disjointedly due to the inherent tissue complexity. In this way, the energy reflected by the tumour is enhanced while the backscattering resulting from the normal healthy tissues is suppressed. Finally, assembling the intensities at all focal points would produce an image, depicting the distributions of energy reflected by a scatterer. The aim of EDAS is primarily to create a pure response signal of the tumor from measured data. Principally the received information includes backscattered signals from malignant breast tissues and clutter (late arrivals) in addition to the backscattered from skin-breast interface and the input signal (early arrivals). Signal processing is used to remove the early arrivals, which dominate the backscattered signals, and filtering them will lead to improving the signal-to-noise ratio of the tumor response. An averaging artifact removal procedure [6, 7] is used to remove the skin artifacts. These artifacts are removed using a calibration process that avoids the use of a breast phantom or *a priori* information. In doing so, a reference signal is created by averaging the recording signals  $Av_{m,n}(t)$ . The reference signal is then subtracted from each of the original recording backscattered signals  $k_{m,n}(t)$ , resulting in the calibrated signals  $x_{m,n}(t)$ , which contain only the tumor response and clutter. Signal averaging is implemented as follows:

$$Av_{m,n}(t) = \frac{1}{s} \sum_{m=1}^M \sum_{n=1}^N k_{m,n}(t) \quad (3)$$

$$x_{m,n}(t) = Av_{m,n}(t) - k_{m,n}(t) \quad (4)$$

where  $M$  is the total number of transmitting antenna,  $N$  the total number of receiving antenna, and  $s = M \times N$  the total number of recorded signals. The round-trip distance from each sensor to the pixel of interest is calculated as shown in Figure 1. This value is then converted into time samples based on the wave propagation speed.

The delay time at each sensor (in unit of samples) can be calculated as follows:

$$\tau_{m,n}(r) = \frac{\|r - r_m\| + \|r - r_n\|}{v\Delta t} \quad (5)$$

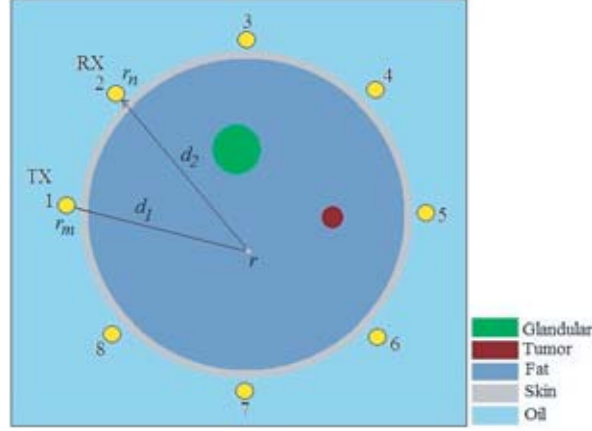


**Figure 1.** Region of interest illustrating distances  $d_1$  and  $d_2$  respectively from transmitter  $r_m$  to focal point  $r$  and back to receiver  $r_n$  [6].

where the speed of propagation is given by:

$$v = \frac{C}{\sqrt{\epsilon_r}} \quad (6)$$

and  $\|r_m - r\|$  and  $\|r_n - r\|$  are the distances between the focal point  $r$  and  $m$ th transmitter and  $n$ th receiver;  $\Delta t$  is the sampling time;  $c$  is the velocity of light in vacuum; and  $\epsilon_r$  is the relative permittivity of the fatty tissue. Following time alignment for each signal recorded at each focal point, a focusing-quality procedure utilizing the coherence factor ( $CF$ ) is implemented. Traditionally, the  $CF$  is used for anomaly correction and side lobe suppression in ultrasound imaging applications [19]. This procedure is based on the utilization of the coherence quality weighting of the backscattered signals at specific focal points inside the domain. The same method can be applied to UWB imaging, which could significantly enhance the image as results from what ultrasonic experiments suggest [17]. In this case, the coherence factor is defined as the ratio of the energy of the coherent sum to the total incoherent energy [20]. Mathematically, the coherence factor  $CF(r)$  is given by:

$$CF(r) = \frac{\text{coherent energy}}{\text{total incoherent energy}} = \frac{\left| \sum_{m=1}^M \sum_{n=1}^N x_{m,n}(t - \tau_{m,n}(r)) \right|^2}{\sum_{m=1}^M \sum_{n=1}^N |x_{m,n}(t - \tau_{m,n}(r))|^2} \quad (7)$$

where  $x_{m,n}(r)$  is a calibrated signal transmitted for the  $m$ th transmitting antenna and  $n$ th receiving antenna;  $\tau_{m,n}(r)$  is the time delay for the  $m$ th transmitting antenna at a point  $r$  and back to the  $n$ th receiving antenna. The focusing quality  $FQ_{m,n}(r)$  is obtained by multiplying the coherence factor with the calibrated signal after time-shifting. Mathematically:

$$FQ_{m,n}(r) = CF(r) x_{m,n}(t - \tau_{m,n}(r)) \quad (8)$$

The high-coherence signals (high coherence factor) represent the main lobe part, which creates an image with good focusing quality, and their amplitude should be maintained. On the other hand, the incoherent signals (low coherence factor) represent the side lobe part, which creates an image with poor focusing quality, and their amplitude should be suppressed. Consequently, the amplitude of each image pixel is adaptively weighted by the corresponding  $CF$  such that the unwanted side lobes are effectively reduced. The enhancement in tumor detection capability of EDAS algorithm is based on the supplementary weighting process involving paring multiplication of the backscattered signals. In this case, each signal pair measured from the same transmitter is multiplied with each other and their products summed. Since this method acquires more information about the targets, extra clutter

elimination is theoretically possible. The multiplication by pair can be expressed as follows:

$$y_{m,n}(r) = \sum_{m=1}^M \sum_{n=1}^{N-1} FQ_{m,n}(r)FQ_{m,n+1}(r) \tag{9}$$

where  $y_{m,n}$  is the output signal after pairing multiplications. Each value of energy is converted into a pixel, and the assembly of these pixels forms an image indicating the location of scatterers.

This procedure is similar to calculating the energy  $En(r)$  at each focal point such that:

$$En(r) = \int_0^w \left[ \sum_{m=1}^M \sum_{n=1}^N y_{m,n}(r) \right]^2 dt \tag{10}$$

and  $w$  is the window length relative to the transmitted pulse width.

### 3. MATERIALS AND METHODS

#### 3.1. Experimental Breast Phantom

The dielectric properties of human tissues at microwave frequencies have been studied in the past where various tissues have been noted to have varying characteristics relating to their water content and structure [21]. A typical adult human breast can be classified into one of the three possible categories depending on the radiographic density. They are (a) fatty, (b) mildly heterogeneous, and (c) densely heterogeneous breasts. Respectively, they are referred herein to as Type A, Type B, and Type C breasts. Figure 2 shows **T1**-weighted magnetic resonance images of the breast types and their corresponding anatomically derived dielectric properties. Examining Figure 2, the high permittivity values of the glandular structures for Type B and Type C can be clearly observed, where values reach a close proximity to those expected for malignant cases.

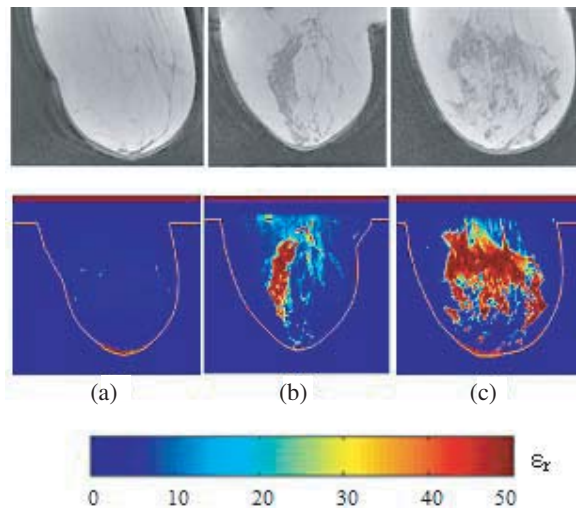


**Figure 2.** T1-MRI (upper) and their corresponding dielectric properties at 5 GHz (lower) of breast classification showing (a) mostly fatty (< 25% glandular) tissue, (b) scattered fibro-glandular tissue (25–50% glandular), and (c) heterogeneously dense breast (51–75% glandular) [5, 21].

The reconstruction of cancerous cells of Type A breast proved to be relatively straightforward as demonstrated by our previous investigations as well as results published by other researchers [22–24]. The challenge is to perform image reconstruction on Type B or Type C breasts due to low contrast between cancerous and glandular structures. In order to investigate the feasibility of the proposed technique in imaging these types of breasts, two heterogeneous breast phantoms were constructed using

mixtures of different chemical materials. These phantoms are similar to some examples reported in previous studies [25] as all materials are dispersive with frequency-dependent characteristics similar to those presented in [5, 26]. The chemical materials and formulas used in the construction of the breast phantom are described [15]. Using these formulas, the phantoms are fabricated composed of skin layer ( $\epsilon_r = 38$ ,  $\sigma = 2 \text{ S/m}$ ), fatty tissue ( $\epsilon_r = 15$ ,  $\sigma = 0.4 \text{ S/m}$ ), and glandular structure ( $\epsilon_r = 32$ ,  $\sigma = 2.5 \text{ S/m}$ ) at the frequency range of 200 MHz to 5 GHz [17]. The methods and procedures used in mixing and preparing the chemicals are identical to those reported elsewhere [24]. Figure 3(b) shows the mildly dense breast model in which the fibro-glandular tissue is simulated by an oval-shape structure of 35 mm in length and 20 mm in width. In this case, the homogenous background constitutes nearly 75% of the total area while the remaining belongs to the inhomogeneous region. This is in agreement with the Type B breast as defined by T1-MRI image in Figure 2(b). Meanwhile, Figure 3(c) shows the heterogeneously dense breast model which comprises two (20 mm radius) circular structures, simulating the fibro-glandular tissues. Here, the homogeneous background occupies approximately 45% of the total area compared to 55% inhomogeneous one. This model agrees with the Type C breast defined by T1-MRI image in Figure 2(c). In both cases, the models are surrounded with 2–3-mm-thick skin tissues and filled with homogeneously fatty material. Meanwhile, the tumors are made from 5 mm-diameter cylindrical structures, and they are fabricated by mixing the right chemicals, so that the formulas result in a mixture with permittivity of 54 at 3 GHz [20]. As shown in Figures 3(a)–(b), each tumor is placed in the fibro-glandular structure of each model, simulating cancerous cells at an early stage of the disease.



**Figure 3.** Fabrication of heterogeneous human breasts based on realistic T1-MRI images: (a) Type B, and (b) Type C models.

### 3.2. Data Acquisition System

The experimental setup showing the important instrumentations and data acquisition system is shown in Figure 5. Referring to Figure 5(a), the data acquisition system is composed of a Cytec CXM 16 multiplexer, to automatically switch transmitting and receiving lines, connected to an Agilent E5071C 8.5 GHz VNA for a frequency sweep of (0–5) GHz providing measurements in the time domain. A wideband 20 dB amplifier is used to improve the received signal power. This acquisition system communicates with a high-end workstation to automate data acquisition and process the reconstruction algorithms.

Figure 4(a) demonstrates the schematic diagram for the experimental setup. Meanwhile, Figure 4(b) shows the actual system including a set of 8 biconical antennas, which are positioned equidistantly around a phantom forming full view geometry. For each antenna position, the  $S_{12}$  signals at each of the receiver locations are sequentially recorded in the time domain. A two-port calibration is performed to minimize insertion losses, impedance mismatch, and electrical delay effects. Figure 5(a) shows the detailed geometrical construction of the UWB antenna with a cone angle of  $45^\circ$  and height of 10 mm driven via a  $50 \Omega$  coaxial feeder, incorporating an in-line ferrite toroid to ensure balanced antenna feeding, through which the RG54 coaxial cable is threaded. The coaxial central core conductor is connected to the apex of the lower cone, while the coaxial outer shield conductor is connected to the upper cone as shown in Figure 5(b). The characteristics of biconical antenna such as  $S_{11}$  is -17 dB, and radiation pattern is 3.62 GHz–9.63 GHz. In the experiments, the sensors are placed in a  $60 \times 60 \times 40$ -cm-size glass tank filled with cooking oil up to 35 cm in height, serving also as a coupling medium between

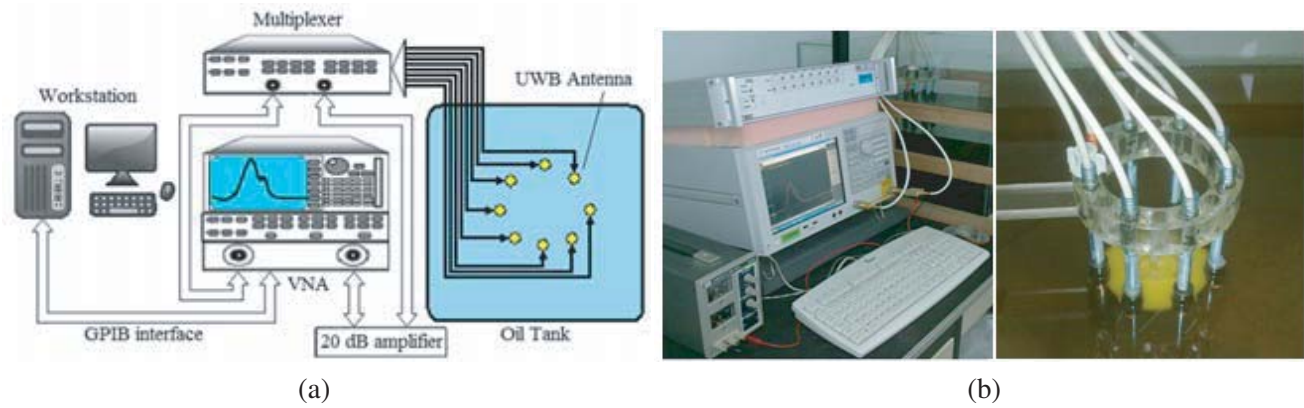


Figure 4. The experimental setup for UWB imaging: (a) schematic diagram, (b) actual system.

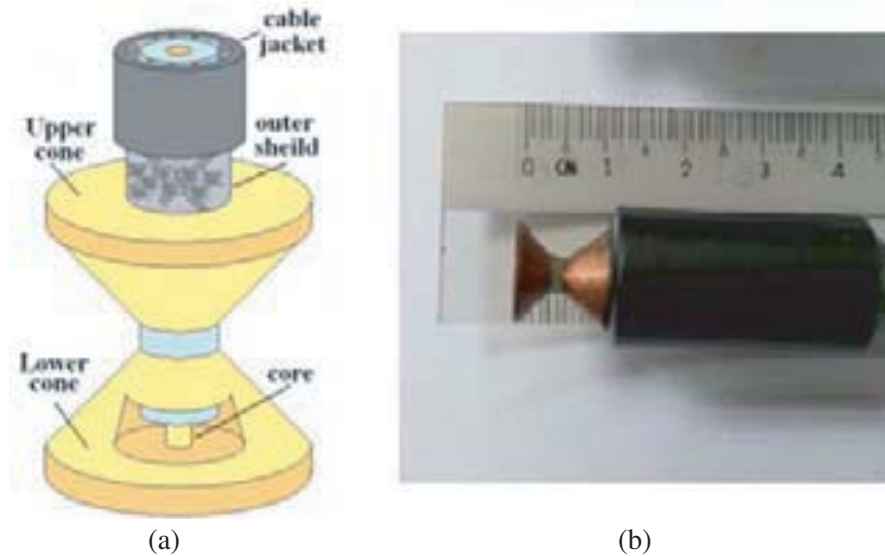
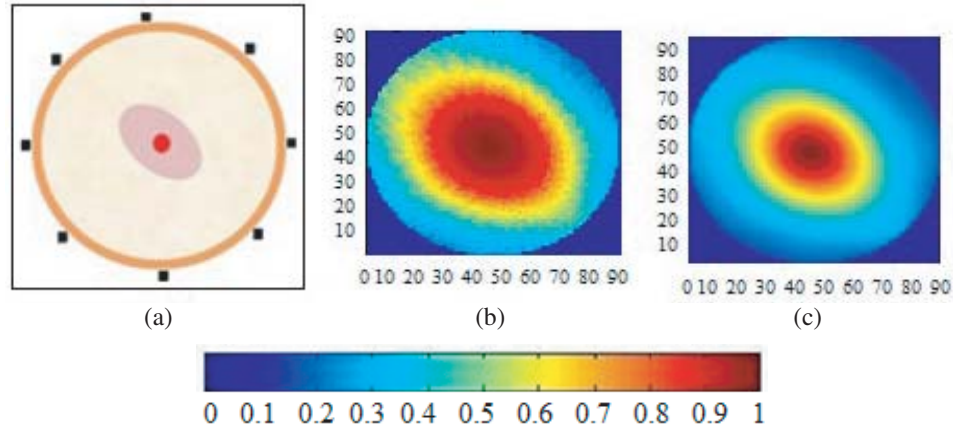


Figure 5. (a) Connection of coaxial cable with the biconical antenna; (b) actual antenna connected with ferrite.

sensors and target. It is found that the liquid similar to oil provides reliable tumor detection and reduces spatial sampling requirements as compared to other immersion media. The antennas were maintained at a constant height of approximately 15 cm below the oil surface. Clutters due to reflections, particularly at the glass-tank and oil-air interfaces, are minimized by appropriate time-gating the arrival pulses.

#### 4. RESULTS AND DISCUSSION

In this study, we present experimental results of ultra-wide band (UWB) imaging comparing qualitative image reconstruction algorithms. The accuracy and fidelity of EDAS are compared with existing delay and sum (DAS) algorithm, namely the classical delay and sum (DAS). In this case, the signal-to-clutter (SCR) ratio has been used to evaluate the performance of the algorithm quantitatively. The SCR is given by ratio of the maximum tumour backscattered energy to the maximum clutter backscattered energy in the same image [9]. Figure 6 shows imaging results reconstructed using Type B breast phantom. Image in Figure 6(b) is reconstructed using DAS. It demonstrates the general capability of the algorithm in distinguishing between tumor and glandular tissue, resulting in SCR values of 2.21 dB. In this case, the image appears blurred, and the size and shape of the glandular region are not properly reconstructed. The result in Figure 6(c) uses the proposed method (EDAS). Clearly this algorithm has resulted in



**Figure 6.** Experimental results of Type B breast phantom with 5 mm tumor embedded inside the glandular region. The actual image is display in (a) while (b) and (c), show reconstructed images using DAS, and EDAS respectively.

an improved reconstruction, registering 4.51 dB in SCR. In this case, the shape and size of tumor as well as the glandular structure have been accurately mapped. In spite of a low contrast ratio, these experiments have proven that the EDAS generally produces a much better reconstruction than DAS technique. Therefore, this image, together with SCR value, serves as reference to the accuracy and reliability of the proposed technique in detecting early stage cancerous cells in the heterogeneous setup.

Figure 7(a) shows the actual image of densely breast model. However, the same observations are not repeated for Type C breast as evident in Figure 7(b)(i). Even though the EDAS algorithm has managed to detect both the tumor and glandular structures, their sizes as well as locations appear distorted. In this case, the SCR ratio of only 1.54 dB was achieved for the 8-antenna geometry. The decrease in the SCR value is partly because the dielectric contrasts between glandular and cancerous tissues are very low, reaching the limit of UWB detection. Another problem is related to the number of unique measurements. In this case, the number of unique measurements is 56 for the 8-antenna system. This corresponds to a spatial resolution to about one-third of the wavelength or approximately equal to 5 mm object size. This figure is slightly lower than the Rayleigh criteria of half of wavelength. One way to overcome this problem is to increase the number of unique measurements by increasing the number of antennas. Our preliminary investigation reveals that the image resolution and the separation distance between objects can be improved to  $\lambda/12$  and  $\lambda/16$ , respectively, if the number of antennas is increased to 16 [27]. In proving this hypothesis, the phantom in Figure 3(b) was scanned again but using a 16-antenna setup, generating 240 unique or independent measurements. Additionally, the phantom was rotated approximately by  $45^\circ$  in order to evaluate the sensitivity of the system in response to position

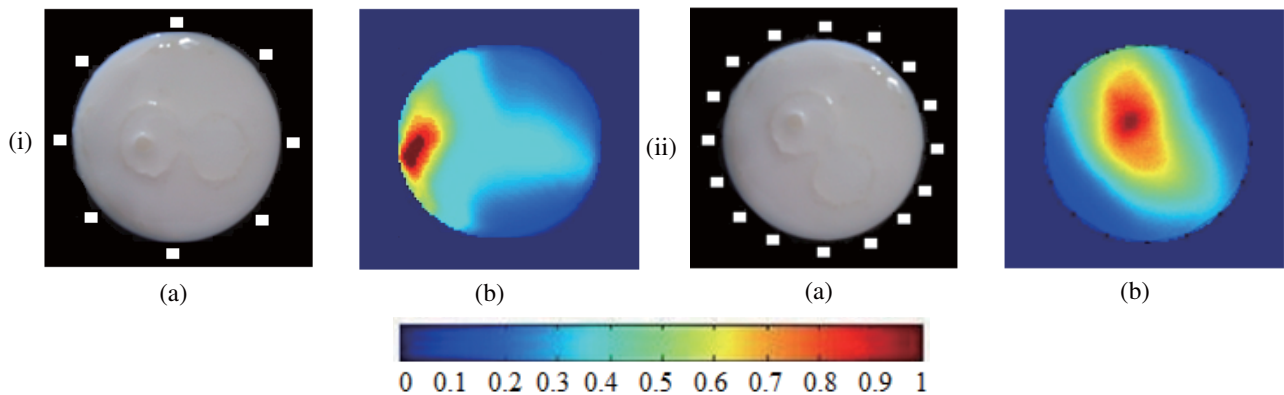


**Figure 7.** Experimental results of densely breast model. (a) Actual image with 5 mm tumor embedded inside the glandular region, (b) reconstruction image of EDAS, (i) using 8 sensors, (ii) using 16 sensors.

variation. The result is displayed in Figure 7(b)(ii).

A close examination of this figure reveals that the tumor detection and its location are significantly enhanced, resulting in improved SCR of 3.12 dB. However, high clutter was still present, causing difficulty in reconstructing the shape as well the size of the scatterers. This shortcoming is principally due to the linear nature of radar-based methods in solving the nonlinear inverse scattering problem. Resultantly, the backscattered energy is very noisy, leading to a reconstruction with a low image-to-noise ratio. The results, therefore, indicate the limitation of applying this imaging modality for cancer detection in heterogeneously dense breast.

## 5. CONCLUSION

In this study, two heterogeneous breast phantoms were experimentally tested to investigate the performance of UWB imaging in detecting cancerous tumors in dense breast tissue. The laboratory phantoms were constructed using chemicals whose dielectric properties closely resembled the actual breast tissues. Experimental results using the MRI-derived breast phantoms indicated that the image produced by the UWB system was comparable with the results obtained from classical DAS method. The reconstruction of UWB imaging for densely heterogeneous glandular breast is more difficult due to the complex distribution of fibro-glandular material, whose dielectric contrast is much smaller than fatty tissues. As the heterogeneity increases, the SCR ratio decreases, presenting a much more challenging imaging scenario. Nevertheless, both the glandular region and cancerous cells have been successfully mapped despite the presence of some artifacts in the image, especially for densely heterogeneous breast. The UWB system together with EDAS algorithm has been shown to provide better resolution, making it possible to distinguish between two scatterers. Considering that the UWB system is relatively safe and cheap, such a system is therefore potentially useful for mass screening or a routine medical examination. However, more research needs to be performed to improve the image-to-noise ratio, especially for the densely heterogeneous breast.

## REFERENCES

1. Hagness, S. C., A. Taflove, and J. E. Bridges, "Two-dimensional FDTD analysis of a pulsed microwave confocal system for breast cancer detection: Fixed-focus and antenna-array sensors," *IEEE Trans. Biomed. Eng.*, Vol. 45, No. 12, 1470–1479, 1998.
2. Moosazadeh, M., S. Kharkovsky, J. T. Case, and B. Samali, "UWB antipodal Vivaldi antenna for microwave imaging of construction materials and structures," *Microwave and Optical Technology Letters*, Vol. 59, No. 6, 1259–1264, 2017.
3. Moosazadeh, M., S. Kharkovsky, Z. Esmati, and B. Samali, "UWB elliptically-tapered antipodal Vivaldi antenna for microwave imaging applications," *IEEE-APS Topical Conference on Antennas and Propagation in Wireless Communications (APWC)*, 102–105, 2016.
4. Winters, D. W., J. D. Shea, P. Kosmas, B. D. Van Veen, and S. C. Hagness, "Three-dimensional microwave breast imaging: Dispersive dielectric properties estimation using patient-specific basis functions," *IEEE Trans. Med. Imag.*, Vol. 28, No. 7, 969–981, 2009.
5. Lazebnik, M., D. Popovic, L. McCartney, C. B. Watkins, M. J. Lindstrom, J. Harter, S. Sewall, T. Ogilvie, A. Magliocco, and T. M. Breslin, "A large-scale study of the ultrawideband microwave dielectric properties of normal, benign and malignant breast tissues obtained from cancer surgeries," *Phys. Med. Biol.*, Vol. 52, 6093–6115, 2007.
6. Li, X. and S. C. Hagness, "A confocal microwave imaging algorithm for breast cancer detection," *IEEE Microw. Wireless Compon. Lett.*, Vol. 11, No. 3, 130–132, 2001.
7. Lim, H. B., N. T. T. Nhung, E. P. Li, and N. D. Thang, "Confocal microwave imaging for breast cancer detection: Delay-multiply-and-sum image reconstruction algorithm," *IEEE Trans. Biomed. Eng.*, Vol. 55, No. 6, 1697–1704, 2008.
8. Yang, F. and A. S. Mohan, "Breast cancer detection: Comparison of data-dependent and data-independent approaches," *2010 Asia-Pacific Microwave Conference Proceedings (APMC)*, 271–274, IEEE, 2010.

9. Byrne, D., M. O'Halloran, M. Glavin, and E. Jones, "Data independent radar beamforming algorithms for breast cancer detection," *Progress In Electromagnetics Research*, Vol. 107, 331–348, 2010.
10. Xie, Y., B. Guo, L. Xu, J. Li, and P. Stoica, "Multistatic adaptive microwave imaging for early breast cancer detection," *IEEE Trans. Biomed. Eng.*, Vol. 53, No. 8, 1647–1657, 2006.
11. Li, J., P. Stoica, and Z. Wang, "On robust Capon beamforming and diagonal loading," *IEEE Trans. Signal Proc.*, Vol. 51, No. 7, 1702–1715, 2003.
12. Nilavalan, R., A. Gbedemah, I. Craddock, X. Li, and S. C. Hagness, "Numerical investigation of breast tumour detection using multi-static radar," *Electron. Lett.*, Vol. 39, 1787–1789, 2003.
13. Bond, E. J., X. Li, S. C. Hagness, and B. D. Van Veen, "Microwave imaging via space-time beamforming for early detection of breast cancer," *IEEE Trans. Antennas Propag.*, Vol. 51, No. 8, 1690–1705, 2003.
14. Lim, H. B., N. T. T. Nhung, E. P. Li, and N. D. Thang, "Confocal microwave imaging for breast cancer detection: Delay-multiply-and-sum image reconstruction algorithm," *IEEE Trans. Biomed. Eng.*, Vol. 55, No. 6, 1697–1704, 2008.
15. Klemm, M., J. Leendertz, D. Gibbins, I. Craddock, A. Preece, and R. Benjamin, "Microwave radar-based breast cancer detection: Imaging in inhomogeneous breast phantoms," *IEEE Antennas Wireless Propag. Lett.*, Vol. 8, 1349–1352, 2009.
16. O'Halloran, M., M. Glavin, and E. Jones, "Channel-ranked beamformer for the early detection of breast cancer," *Progress In Electromagnetics Research*, Vol. 103, 153–168, 2010.
17. Porter, E., J. Fakhoury, R. Oprisor, M. Coates, and M. Popovic, "Improved tissue phantoms for experimental validation of microwave breast cancer detection," *Proc. of the Fourth European Conf. on Antennas and Propagation*, 1–5, Barcelona, Spain, 2010.
18. Hollman, K., K. Rigby, and M. O'Donnell, "Coherence factor of speckle from a multi-row probe," *Proc. IEEE Ultrasonic Symp.*, 1257–1260, Caesars, Tahoe, NV, 1999.
19. Wang, S. L., C. H. Chang, H. C. Yang, Y. H. Chou, and P. C. Li, "Performance evaluation of coherence-based adaptive imaging using clinical breast data," *IEEE Trans. Ultrason. Ferroelectr. Freq. Control*, Vol. 54, No. 8, 1669–1679, 2007.
20. Campbell, A. and D. Land, "Dielectric properties of female human breast tissue measured in vitro at 3.2 GHz," *Phys. Med. Biol.*, Vol. 37, No. 1, 193, 2000.
21. Zastrow, E., S. K. Davis, M. Lazebnik, F. Kelcz, B. D. Van Veen, and S. C. Hagness, "Development of anatomically realistic numerical breast phantoms with accurate dielectric properties for modeling microwave interactions with the human breast," *IEEE Trans. Biomed. Eng.*, Vol. 55, No. 12, 2792–2800, 2008.
22. Leendertz, J., A. Preece, R. Nilavalan, I. Craddock, and R. Benjamin, "A liquid phantom medium for microwave breast imaging," *6th International Congress of the European Bioelectromagnetics Association, Budapest, Hungary*, 2003.
23. Sill, J. M. and E. C. Fear, "Tissue sensing adaptive radar for breast cancer detection-experimental investigation of simple tumor models," *IEEE Trans. Microwave Theory Tech.*, Vol. 53, No. 11, 3312–3319, 2005.
24. Zanoon, T. and M. Abdullah, "Early stage breast cancer detection by means of time-domain ultra-wide band sensing," *Meas. Sci. Technol.*, Vol. 22, 114016, 2011.
25. Hahn, C. and S. Noghianian, "Heterogeneous breast phantom development for microwave imaging using regression models," *Journal Biomed. Imag.*, Vol. 2012, 6, 2012.
26. Lazebnik, M., E. L. Madsen, G. R. Frank, and S. C. Hagness, "Tissue-mimicking phantom materials for narrowband and ultrawideband microwave applications," *Phys. Med. Biol.*, Vol. 50, 4245–4258, 2005.
27. Zanoon, T. F., M. S. Hathal, and M. Abdullah, "Microwave imaging at resolution and super-resolution with ultra-wide band sensors," *2012 IEEE Int. Conf. Imaging Systems and Techniques (IST)*, 538–543, IEEE, 2012.